Indian Journal of Engineering & Materials Sciences
Vol. 30, August 2023, pp. 629-645
DOI: 10.56042/ijems.v30i4.5038

A Comparative Study of the Dynamic Stability of a Rotor Supported by an Air-Bearing and an Air-ring Bearing

Muruganandam Muthanandam*

Department of Mechanical Engineering, PSN College of Engineering and Technology, Tirunelveli 627 152, India

Received: 22 July 2022; Accepted: 2 August 2023

An exploration to justify the need for an air-ring around an air-bearing is done by comparing the dynamic stability plots of a rotor supported by air-bearings with and without an air-ring. Air-bearing with air-ring or air-ring bearing has pocketed feed-holes. The air-bearing without air-ring has plain feed-holes and it is referred to as air-bearing with a direct feeding system. A linearized free-vibration model rotor-bearing is used to analyze the dynamic stability. The dynamic coefficients of air-bearing with a direct feeding system and air-ring bearing are affected by whirl frequency due to the fluid compressibility effects. The stability threshold speed of the rotor air-ring bearing system is increased well above the threshold speed of the rotor air-bearing with a direct feeding system. The rotor critical mass of the rotor air-ring bearing system is smaller than that of the rotor air-bearing with a direct feeding system. The air-ring of air-ring bearing can prevent self-excited vibration in lightly loaded rotor-bearing systems.

Keywords: Dynamic coefficients, Gas-lubricated, Hydrostatic journal bearing, Self-excited vibration, Stability threshold speed

1 Introduction

Air bearings are suitable for supporting high-speed, lightly loaded rotors such as micro-gas turbines, heat pumps, injection systems in automotive engines, grinding machines, special machine tools, gyros, magnetic heads in computer hard discs, dental drills, and micro-air vehicles, etc.

The following two kinds of dynamic instabilities are considered to design a journal air bearing for a given rotor[1]: synchronous whirl and self-excited whirl. Gross[2] proved using both theory and experiments that the self-excited whirl was more predominant in air-lubricated bearings than in oil-lubricated bearings. Most of the research attempts on air bearings have been to analyze and evaluate this second kind of dynamic instability. Dynamic stability analysis of a symmetrical and flexible rotor supported by plain cylindrical gas bearings which in turn were mounted on flexible and damped supports was reported.[3] Three different methods such as the frequency response method, nonlinear orbit approach, and response to a step-jump method were used to determine the stability of a gas-lubricated tilting-pad journal bearing.[4] Powell & Tempest[5] demonstrated that an introduction of an O-ring as bushing support resulted in self-excited whirl stabilization. The use of air as compared to a conventional lubricant such as oil has a detrimental effect on air-bearing operations. The lower viscosity and smaller damping capacity of air result in self-excited vibration.[6] A linearized theory of self-excited vibration analysis on noncircular bearings and flexibly mounted bearings was presented.[7] Majumdar[8] derived an equation of angular whirl frequency by a stability analysis of a rotor-bearing system with O-rings-supported bushings. The analytical results of Majumdar[8] were in good agreement with the experimental findings of Powell & Tempest[5]. In a parametric study of conical whirl instability on porous gas journal bearings[9], at the threshold condition, the angular velocity of the journal center ν was determined to lie between 0.498 and 0.504 of the angular velocity of the rotor ω.

Otsu *et al.*[10] investigated the dynamic instability of a rigid rotor supported by aero-static bearings with compound restrictors. Bonello & Pham[11] presented a generic technique for the transient nonlinear dynamic analysis and the static equilibrium stability analysis of a turbomachine running on foil air bearings. Arghir *et al.*[12] examined the pneumatic hammer instability in an aero-static bearing with shallow recesses and orifices using computational fluid dynamics analysis and experiments on a floating bearing test rig. Xiao *et al.*[13] analyzed aero-static journal millimeter-scale

*Corresponding author (Email: m.muruganandam@psncet.ac.in)

micro-bearings with the perspectives of restriction, structure, and operation parameters. Several novel designs of aerostatic bearings such as Sixsmith, bushing with tangential orifices, and dual gas film or externally-pressurized journal air-bearing (AB) with an air-ring (AR), or air-ring bearing (ARB) (Fig. 1) were proposed.[14] Zeise & Schweizer[15] made the dynamic stability analyses of a rotor supported by air foil bearings where a rigid ring separates the air film from the elastic foil structure.

Brzeski & Kazimierski[16] explained the configuration of an ARB and its general operating principle. Kazimierski & Trojnarski[17] presented the theoretical models for computing the mass flow rate of air through the plain feed-hole and the pocketed feed-hole in ARB. Czołczyński *et al.*[18] analyzed the dynamic response of ARB to a step-change in force. A single-degree-of-freedom approach for determining the dynamic coefficients (DC), such as stiffness coefficients and damping coefficients, of ARB, was presented by Czołczyński.[19] In a single-degree-of-freedom approach, the geometric center of the journal (CG_J) was prescribed to follow a simple harmonic motion (SHM) to determine the DC of AB, by fixing the position of the bushing center (CG_B). Similarly, by securing the position of CG_J, CG_B was allowed to follow an SHM to determine the DC of AR. In this approach, analysis for the pressure (p) distribution in the AB and AR regions (Fig. 1) were made by solving Reynolds' equation separately in each region, and thereby their DC were determined separately. The range of values of DC for an ARB that would enable dynamic stability of a symmetrically loaded, rigid rotor was estimated by Czołczyński *et al.*.[20] Czołczyński[21,22] presented the results of numerical experiments on the dynamic stability of the rotor air-ring bearing system (RARBS). By following the methods of Czołczyński[22], Muthanandam *et al.*[23,24] presented the analysis of an ARB.

The previous studies[16–24] analyzed the dynamic stability of RARBS and the rotor air-bearing with a direct feeding system (RABDFS). In these studies, the DC of ARB and the DC of air-bearing with a direct feeding system (ABDFS) were determined using a single-degree-of-freedom approach. Muthanandam & Thyageswaran[25] determined the DC of ARB using a two-degrees-of-freedom approach. This paper analyzes the dynamic stability of the RARBS and the RABDFS where the DC of ARB and the DC of ABDFS are determined using the two-degrees-freedom approach. In a two-degrees-of-freedom approach, the motion of CG_B is linked to the motion of CG_J. The differential equations of motion of air, through the feed-hole passages, AR, and AB regions were solved via a three-dimensional computational fluid dynamics analysis. The DC of AR and AB were determined simultaneously.

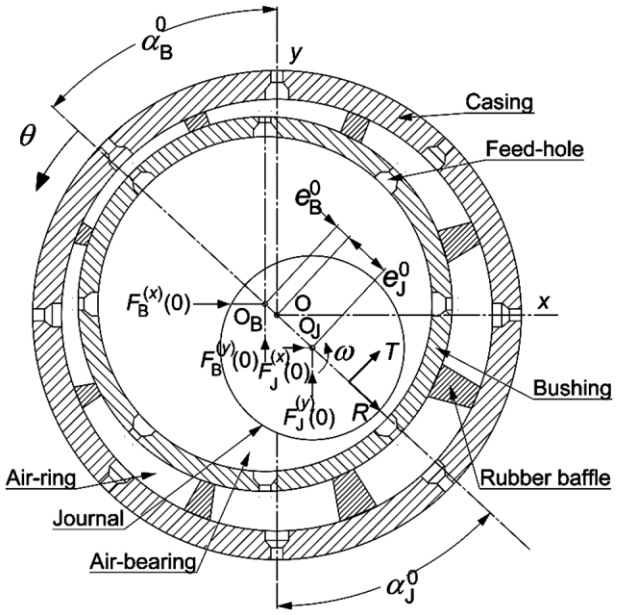

Fig. 1 — Air-ring bearing at static equilibrium conditions.

2 Materials and Methods

2.1 Dynamic stability analysis of ARB

2.1.1 Outline

The objective of this paper is to ascertain the need for an AR in an AB. In this paper, a comparative study of the dynamic stability against self-excited whirl of a balanced, rigid, and light-weight rotor having symmetrical loading (Fig. 2) supported by the following types of air-bearings is carried out: (a) ARB (Fig. 3) and (b) ABDFS (Fig. 4).

The dynamic stability analysis is made when the rotor of RARBS rotates at ω and occupies a static equilibrium position as shown in Fig. 1. The static equilibrium position of the CG_J is O_J. It is defined in terms of eccentricity (e) and attitude angle (α) as $\left(e_J^0, \alpha_J^0\right)$. In this condition, the CG_B occupies O_B. It is defined in terms of e and α as $\left(e_B^0, \alpha_B^0\right)$. The components of static load-carrying capacity are $\left(F_J{}^{(x)}(0), F_J{}^{(y)}(0)\right)$ and $\left(F_B{}^{(x)}(0), F_B{}^{(y)}(0)\right)$. The subscripts J and B in $F_J{}^{(i)}(0)$ and $F_B{}^{(i)}(0)$ are used to indicate the bearing forces in direction i, on journal and bushing respectively. i can be x or y.

The dynamic stability of the RABDFS and the RARBS are verified by solving the equations of free-vibration of the RABDFS and the RARBS respectively. A complete dynamic stability analysis requires the determination of DC at all ω and ν in the range of $1 \le \omega$ (rad s^{-1}) ≤ 2565.6 and $1 \le \nu$ (rad s^{-1}) ≤ 1282.8. $\omega_{max} = 2565.6$ rad s^{-1} corresponds to the maximum rotor speed, $S_{max} = 24500$ RPM (see Table 1). Since the problem considered here investigates self-excited vibration or half-frequency whirl, $\nu_{max} = \omega_{max}/2 = 1282.8$ rad s^{-1}. Since the dynamic stability of a rotor AB system depends on the DC of an AB and again since the DC depend on ω and ν, either a map of the DC (Type1 dynamic stability map) or a map of ω and ν (Type 2 dynamic stability map) can be arrived at by solving the equations of motion. These maps dictate the range of DC (for Type 1) and the range of ω and ν (for Type 2), at which the rotor AB system is dynamically stable.

Table 1 — Rotor air-bearing system configurations

	RABDFS	RARBS
m_R (kg)	3.42	3.42
$I_{d,R}$ (kg m^2)	0.0283	0.0283
$I_{p,R}$ (kg m^2)	0.0012	0.0012
m_{JB} (kg)	0.925	0.925
$I_{d,JB}$ (kg m^2)	0.0076	0.0076
l (m)	0.09	0.09
D_J (mm)	20	20
L (mm)	20	20
c_{AB} (μm)	11	11
D_B (mm)	—	44
c_{AR} (μm)	—	15
D_C (mm)	100	100
r	2	2
n	8	8
d_o (mm)	0.1	0.1
h_o (mm)	0.1	0.1
h_{do} (mm)	0.16	0.16
d_c (mm)	—	0.9
h_c (mm)	—	1
$d_{FH,\,AB}$ (mm)	0.5	0.5
$d_{FH,\,AR}$ (mm)	—	4
γ (rad)	—	0.1047
β (rad)	—	0.3403
p_s (bar)	7.01	7.01
T_s (K)	333	333
S_{max} (RPM)	24500	24500

2.1.2 Geometrical configuration of air-ring bearing

Figures 2 & 3 show the RARBS being analyzed in this research. The rotor (R) of mass m_R is supported on the ARB, as shown in Fig. 2. Figures 3(a) & 3(b) show the longitudinal section and the cross-section of the ARB, respectively. The ARB consists of two cylindrical bushings (B) of total mass m_{JB} joined with each other using connectors to form a joint-bushing (JB). The joint-bushing is assembled with a casing (C) with a clearance fit using rubber seals and rubber baffles. Parts B and C have radial feed-holes for supplying compressed air to the ARB. There are two rows of feed-holes, with eight feed-holes per row. The first row of feed-holes is provided in C and B at distances of $L/6$ and $L/4$, respectively, where L is the length of the journal bearing (see Fig. 3(a)). The second row of feed-holes is provided in C and B at $5L/6$ and $3L/4$, respectively. Air at supply pressure p_s enters the feed-holes provided in C before it flows through the AR and into the feed-holes in B. It then flows in the AB and is exhausted into the

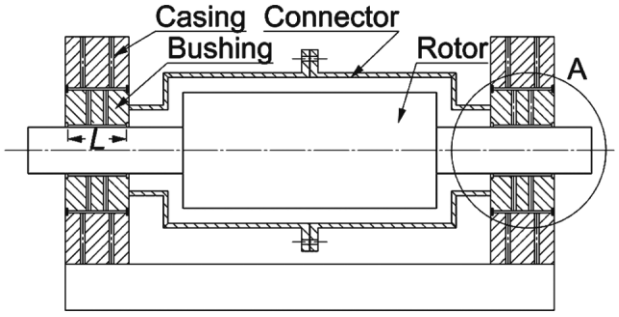

Fig. 2 — Rotor air-bearing system.

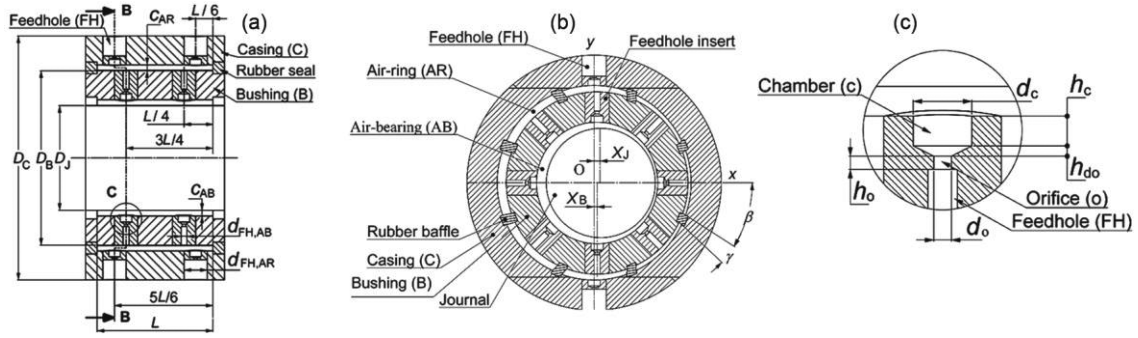

Fig. 3 — (a) Longitudinal-section of air-ring bearing (Detail A of Fig. 2), (b) Cross-section of air-ring bearing (Section B-B of Fig. 3(a)) & (c) Cross-section of feed-hole (Detail C of Fig. 3(a)).

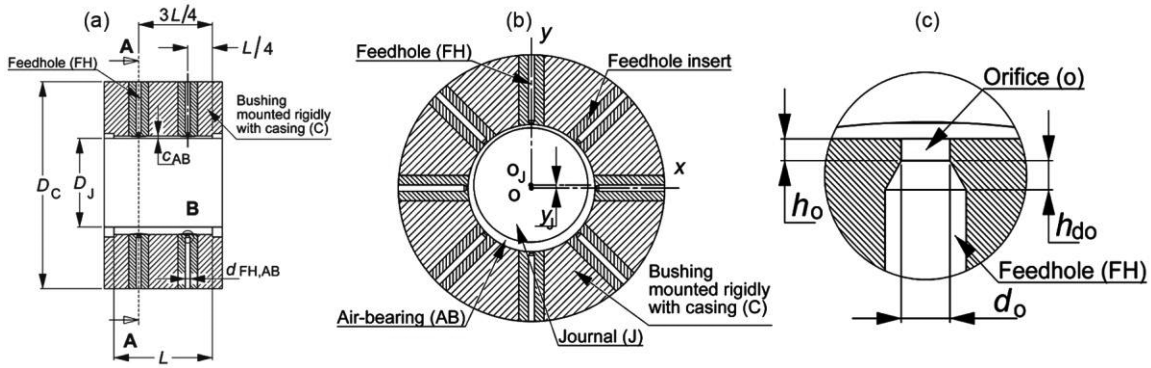

Fig. 4 — (a) Longitudinal-section of air-bearing with a direct feeding system (Detail A of Fig. 2), (b) Cross-section of air-bearing with a direct feeding system (Section A-A of Fig. 4(a)), (c) Cross-section of feed-hole (Detail B of Fig. 4(a)).

atmosphere through the bearing ends. p_s is selected based on the delivery p of a commercially available screw compressor. Figure 3(c) shows the geometry of the feed-hole in B and C.

2.1.3 Geometrical configuration of air-bearing with a direct feeding system

Figure 4 shows the ABDFS. Figures 4(a) & 4(b) show the longitudinal section and the cross-section of the ABDFS, respectively. The rotor (R) of mass m_R is supported on the ABDFS, as shown in Fig. 2 except that the bushing of the ABDFS is rigidly mounted with the casing (C). Part C has radial feed-holes for supplying compressed air to the AB. There are two rows of feed-holes, with eight feed-holes per row. The first row and the second row of feed-holes are provided in C at distances of $L/4$ and $3L/4$, respectively, where L is the length of the journal bearing (see Fig. 4(a)). Air at p_s enters the feed-holes provided in C before it flows through the AB and is exhausted into the atmosphere through the bearing ends. p_s is selected based on the delivery p of a commercially available screw compressor. Figure 4(c) shows the geometry of the feed-hole in C.

The details of the geometry and operating conditions of RARBS and RABDFS configurations are given in Table 1.

2.1.4 Determination of dynamic coefficients of RABDFS and RARBS

The system constants m_R, m_{JB}, and the DC of AB, AR, and elastomeric support (ES), i.e., K_{AB}, K_{AR}, K_{ES}, C_{AB}, C_{AR}, C_{ES}, respectively, are used to characterize the idealized RARBS. The rotor load $P_R = m_R g/2$ and the joint-bushing load $P_{JB} = m_{JB} g/2$ (see Fig. 5). The bushing support (BS) shown in Fig. 5 has two elements such as AR and ES which operate in a parallel arrangement as shown in Fig. 6(a). The DC of

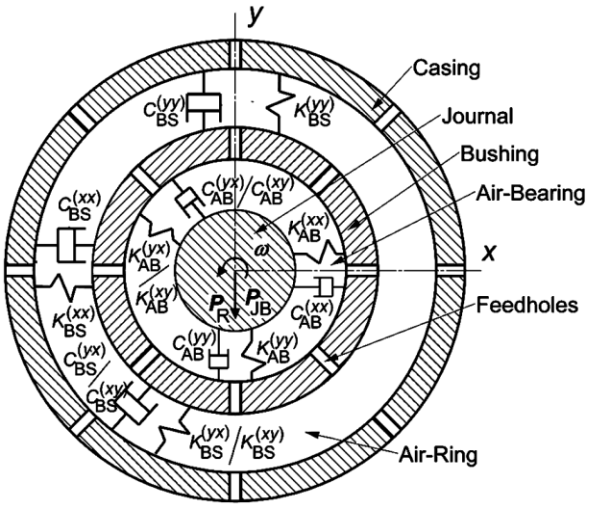

Fig. 5 — Idealized physical model of RARBS.

BS, AR, and ES are related by $K_{BS} = K_{AR} + K_{ES}$ and $C_{BS} = C_{AR} + C_{ES}$. The DC of ES were measured in $314.2 \leq \nu\,(\text{rad s}^{-1}) \leq 6283.2$ and reported by Smalley *et al.*[26] and Al-Bender *et al.*[27]. Measurements on various sizes of O-rings made of materials such as Viton 75, Viton 90, Kalrez 4079, and Kalrez 6375 show that $K_{ES,avg} = 10.542 \times 10^6$ N m^{-1} and $C_{ES,avg} = 5531.5$ N s m^{-1}. Muthanandam & Thyageswaran[25] showed that $K_{AR,avg}^{(xx)} = 31.152 \times 10^6$ N m^{-1} and $C_{AR,avg}^{(xx)} = 23181.8$ N s m^{-1} in $340.3 \leq \nu\,(\text{rad s}^{-1}) \leq 1282.2$. Thus, it is found that the DC of ES are smaller than the DC of AR reported by Muthanandam & Thyageswaran[25], i.e., $K_{ES,avg}/K_{AR,avg} = 0.3384$ and $C_{ES,avg}/C_{AR,avg} = 0.2386$. The results of DC of AR justify the simplification assumptions $K_{BS} \cong K_{AR}$ and $C_{BS} \cong C_{AR}$ made in the two-degrees-of-freedom procedure presented by Muthanandam & Thyageswaran[25]. Hence, for evaluating the stability of RARBS in this paper, only the DC of AR is

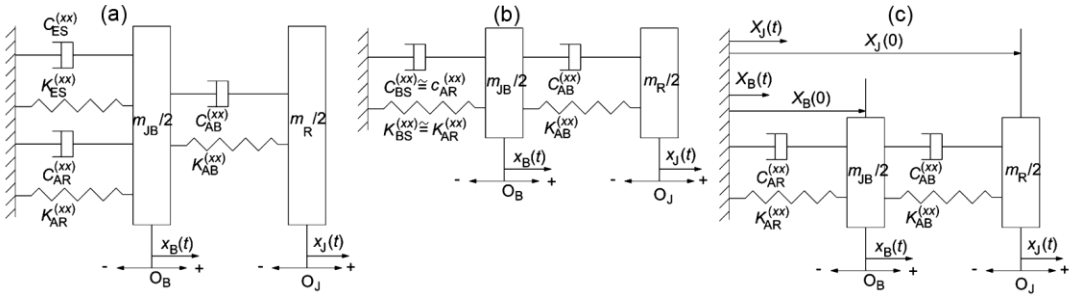

Fig. 6 — Idealized physical model of RARBS (Showing stage-1 of transient-state simulation of two-degrees-of-freedom approach).

considered and the DC of ES is neglected. i.e., $K_{BS} \cong K_{AR}$ and $C_{BS} \cong C_{AR}$ as shown in Fig. 6(b). These approximations to K_{BS} and C_{BS} are done to simplify the two-degrees-of-freedom approach which involves only a fluid dynamic analysis. If the DC of seals and rubber baffles (see Fig. 3) are also considered then a combined fluid-structural dynamic analysis would become necessary. Such an exercise has not been attempted in this research.

At time t = 0 of a two-degrees-of-freedom approach[25], the transient-state simulation (TSS) starts from the static equilibrium position of CG_J (O_J) and CG_B (O_B) as shown in Fig. 6(c). The incremental displacements of CG_J at any t are: $x_J(t) = X_J(t) - X_J(0)$, $y_J(t) = Y_J(t) - Y_J(0)$. Similar expressions can be set up for CG_B measured about the static equilibrium position. Together, these form the elements of x_J, y_J, x_B, and y_B. The TSS consists of two stages: In stage 1, CG_J is simulated to follow an SHM i.e., $x_J(t) = A \sin(\nu t)$ with $y_J(t) = 0$. In stage-2, $x_J(t) = 0$ with $y_J(t) = A \sin(\nu t)$. Due to the movement of CG_J, the instantaneous distribution of p around the bushing in both AB and AR shall determine the instantaneous position of the CG_B i.e., $(X_B(t), Y_B(t))$. When the TSS is conducted with a time-step $\Delta t = 2\pi/(\nu N)$, where N is the number of time steps in one period, it provides data to form the vectors of incremental displacements: x_J, y_J, x_B, y_B; incremental velocities: $\dot{x}_J, \dot{y}_J, \dot{x}_B, \dot{y}_B$; and absolute dynamic load-carrying capacities: $F_J^{(ij)}, F_B^{(ij)}$. The superscripts i and j in $F_J^{(ij)}$ and $F_B^{(ij)}$ are used to indicate the bearing forces on the journal and bushing respectively, in direction i when CG_J moves along direction j. The procedure of computing $F_J^{(ij)}$ and $F_B^{(ij)}$ in the two-degrees-of-freedom solution approach was explained by Muthanandam & Thyageswaran[25]. There are N+1 elements in x_J, i.e., $x_J(t_n) = \{x_J(t_0), x_J(t_1), x_J(t_2), \ldots x_J(t_N)\}$, where $t_n = n\Delta t$ and n = 0, 1, 2 … N. Velocity $\dot{x}_J$ and acceleration $\ddot{x}_J$ can then be found from x_J by time-differentiation. Similar N+1 elements can be envisaged for y_J, x_B, y_B, $\dot{y}_J$, $\dot{x}_B$, $\dot{y}_B$, $\ddot{y}_J$, $\ddot{x}_B$, $\ddot{y}_B$, $F_J^{(ij)}$, and $F_B^{(ij)}$. Components of incremental dynamic load-carrying capacity $f_J^{(xj)}$ and $f_J^{(yj)}$ are: $f_J^{(xj)}(t) = F_J^{(xj)}(t) - F_J^{(x)}(0)$ and $f_J^{(yj)}(t) = F_J^{(yj)}(t) - F_J^{(y)}(0)$, where j can be x or y. Similar sets of expressions can be written for $f_B^{(xj)}$ and $f_B^{(yj)}$. Time-series of incremental displacement, incremental velocity, and incremental load-carrying capacity obtained by TSS are used to evaluate the DC of AR and AB in a coupled manner.[25]

The superscripts i and j in DC of AB and AR are used to indicate the bearing forces of AB and AR respectively, in direction i when CG_J moves along direction j. The superscripts i and j in DC can be x or y as in Fig. 5; for example, when i is x and j is y, $K_{AR}^{(ij)} = K_{AR}^{(xy)}$, $C_{AB}^{(ij)} = C_{AB}^{(xy)}$ etc. The DC of ARB depend on $F_J^{(y)}(0)$, $F_B^{(y)}(0)$, ω, and ν, and can be used to form the equations of motion of the journal and bushing. The equations of motion of the rotor and the joint-bushing around their static equilibrium positions in the RARBS have been derived elsewhere.[28] The analyses of these equations of motion are done using a state-space form, a set of the first-order ODE, one for each state.[28] Upon solving these equations, the stability of the rotor supported in the ARB near its static equilibrium position can be analyzed, and ω_{DSB} of the rotor can be determined. The DC of ABDFS depend on $F_J^{(y)}(0)$, ω, and ν, and can be used to form the equations of motion of the journal. Upon solving these equations, the stability of the rotor supported in the ABDFS near its static equilibrium position can be analyzed, and ω_{DSB} of the rotor can be determined.

Determining the DC of an AB at all ω and ν in its operating range would be impractical if not

impossible. The DC of an AB at any ω and ν in its operating range can be estimated by following the steps: (a) Determining the DC of AB at all sets of M selected values of ω and N selected values of ν in the operating range using the two-degrees-of-freedom approach presented by Muthanandam & Thyageswaran[25]; (b) Estimating the DC at any ω and ν in its operating range by following a procedure of two-dimensional interpolation for (ω, ν) using $M \times N$ sets of DC. An interpolation procedure[22] using a finite Fourier series of ω and ν is employed in this research.

2.1.5 Dynamic stability analyses of RABDFS and RARBS

The dynamic stability analysis is made by scanning ω and ν in the range of $1 \le \omega$ (rad s^{-1}) ≤ 2565.6 and $1 \le \nu$ (rad s^{-1}) ≤ 1282.8. ω_{max} = 2565.6 rad s^{-1} corresponds to the maximum rotor speed, S_{max} = 24500 RPM (Table 1). Since the problem considered here investigates self-excited vibration or half-frequency whirl, $\nu_{max} = \omega_{max}/2$.

Calculation procedure for type 1 dynamic stability map of RABDFS when elastomeric support is introduced between the bushing and the casing

When elastomeric support (ES) is introduced between the bushing and the casing of an ABDFS, the type 1 dynamic stability map of the DC of ES can be obtained. The calculation procedure is as follows (see Fig. 7):

i. m_R, m_{JB}, $I_{d,R}$, $I_{d,JB}$, $I_{p,R}$, and l (see Table 1) are defined.
ii. There are 25 sets of (ω, ν) where the DC of AB are determined by following the two-degrees-of-freedom solution procedure presented by Muthanandam[28].
iii. The initial values of DC of ES for bushing, $K_{ES}^{(xx)}$ and $C_{ES}^{(xx)}$, ω, and ν are assigned.
iv. Using the map of identified DC of AB at M selected values of ω and N selected values of ν in the operating range, the DC of AB at any ω and ν are calculated.[28]
v. Using the DC of ES and AB, eigenvalues $\lambda = \eta \pm i\zeta$ are computed.[28]
vi. Steps (4) and (5) are executed by incrementing ω, ν, and the DC of ES. If $\nu = \nu_{max}$ and $\omega = \omega_{max}$ then the values of DC of ES are incremented. $\Delta K_{ES}^{(xx)}$ and $\Delta C_{ES}^{(xx)}$ are dictated by the scale of $K_{AR}^{(xx)}$ and $C_{AR}^{(xx)}$ presented by Muthanandam & Thyageswaran[25].
vii. At given $K_{ES}^{(xx)}$ and $C_{ES}^{(xx)}$, if $\eta > 0$ and $\omega \neq \omega_{LDSB}$, the lower dynamic stability threshold speed, then the value of ω is incremented. Steps (4) and (5) are executed. If $\eta > 0$ then the rotor-bearing system is dynamically unstable at the given ω and ν for the given DC of ES and AB.
viii. At a given $K_{ES}^{(xx)}$ and $C_{ES}^{(xx)}$, if $\eta < 0$ then the rotor-bearing system is dynamically stable at the given ω and ν for the given DC of ES and AB.$\omega = \omega_{LDSB}$.
ix. At a given $K_{ES}^{(xx)}$ and $C_{ES}^{(xx)}$, if $\eta < 0$ and $\omega > \omega_{LDSB}$ then the value of ω is incremented. Steps (4) and (5) are executed.
x. At a given $K_{ES}^{(xx)}$ and $C_{ES}^{(xx)}$, if $\eta > 0$ and $\omega > \omega_{LDSB}$ then the rotor-bearing system is dynamically unstable at the given ω and ν for the given DC of ES and AB. $\omega = \omega_{UDSB}$, the upper dynamic stability threshold speed.
xi. The maps of DC of ES for bushing, $K_{ES}^{(xx)}$ and $C_{ES}^{(xx)}$, for which the rotor-bearing system is dynamically stable at all ω and ν in the operating range is arrived at.

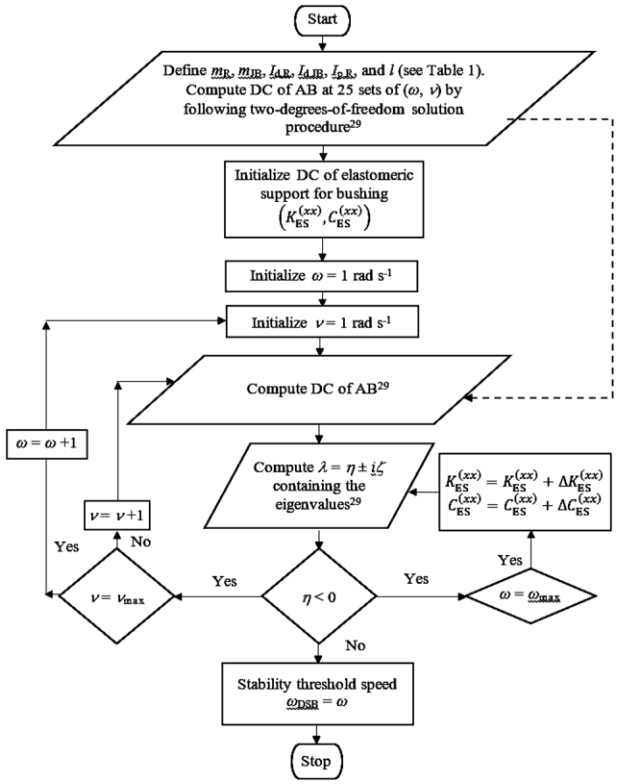

Fig. 7 — Calculation procedure for type 1 dynamic stability map of DC of ES for RABDFS.

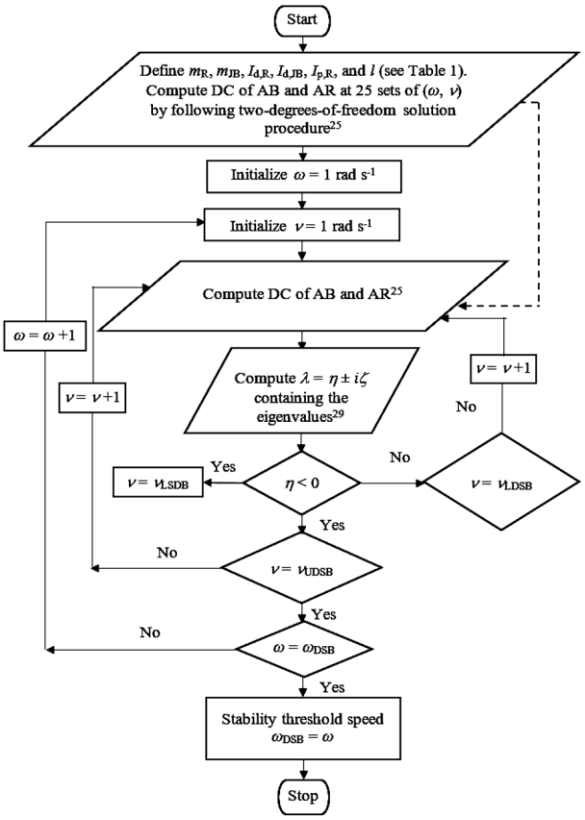

Fig. 8 — Calculation procedure for type 2 dynamic stability map of RARBS.

Calculation procedure for type 2 dynamic stability map of RARBS

The calculation procedure, for the type 2 dynamic stability map of RARBS, is as follows (Fig. 8):

i. m_R, m_{JB}, $I_{d,R}$, $I_{d,JB}$, $I_{p,R}$, and l (Table 1) are defined.
ii. There are 25 sets of (ω, ν) where the DC of AB and AR are determined by following the two-degrees-of-freedom solution procedure presented by Muthanandam & Thyageswaran[25].
iii. The initial values of ω and ν are assigned.
iv. Using the map of identified DC at M selected values of ω and N selected values of ν in the operating range, the DC of AB and AR at any ω and ν are calculated.[28]
v. Using the DC of AB and AR, $\lambda = \eta \pm i\zeta$ are computed.[28]
vi. ω is incremented and steps (4) and (5) are executed.
vii. At a given ω, if $\eta > 0$ and $\nu \neq \nu_{LDSB}$, the lower dynamic stability threshold frequency, then the value of ν is incremented. Steps (4) and (5) are executed. If $\eta > 0$ then the rotor-bearing system is dynamically unstable at the given ω and ν for the given DC of AB and AR.
viii. At a given ω, if $\eta < 0$ then the rotor-bearing system is dynamically stable at the given ν for the given DC of AB and AR. $\nu = \nu_{LDSB}$.
ix. At a given ω, if $\eta < 0$ and $\nu > \nu_{LDSB}$ then the value of ν is incremented. Steps (4) and (5) are executed.
x. At a given ω, if $\eta > 0$ and $\nu > \nu_{LDSB}$ then the rotor-bearing system is dynamically unstable at the given ν for the given DC of AB and AR. $\nu = \nu_{UDSB}$, upper dynamic stability threshold frequency.
xi. At a given ω, if $\eta > 0$ for all ν then the rotor-bearing system is dynamically unstable for the given DC of AB and AR. $\omega = \omega_{DSB}$, stability threshold speed.
xii. The maps of ω and ν for which the rotor-bearing system is dynamically stable are arrived at.

Calculation procedure for rotor critical mass and whirl frequency at the threshold of dynamic instability at a given speed

The dynamic stability analysis is made when the rotors of RABDFS and RARBS rotate at ω and occupy $\left(e_J^0, \alpha_J^0\right)$. In the RARBS, the bushing occupies $\left(e_B^0, \alpha_B^0\right)$. Let the rotor be excited to whirl about this condition with a ν. If the vibration amplitude remains constant with time as in a neutral stable condition, then the rotor is at the threshold of dynamic instability. The rotor mass, for which it remains in a neutral stable condition at ω, is known as the rotor critical mass ($m_{R,C}$). Stability threshold whirl frequency, ν_{DSB}, and $m_{R,C}$ are determined by varying ν over a given range $1 \leq \nu \leq \nu_{max}$ where $\nu_{max} = \omega_{max}/2$. The determinant of the overall system of equations of motion can be arrived at[3] as given below.

$$\begin{vmatrix} A & B \\ C & D \end{vmatrix} = 0 \qquad \ldots (1)$$

where

$$A = K_{AB,ND}^{(xx)} + i\varsigma C_{AB,ND}^{(xx)} - \frac{\kappa}{1 - \frac{\kappa}{K_{AR,ND}^{(xx)} - K_{R,ND}\left(\frac{m_{JB,ND}}{2}\right)\kappa + i\varsigma C_{AR,ND}^{(xx)}}}$$

$$B = K_{AB,ND}^{(xy)} + i\varsigma C_{AB,ND}^{(xy)}$$

$$C = K_{AB,ND}^{(yx)} + i\varsigma C_{AB,ND}^{(yx)}$$

$$D = K_{AB,ND}^{(yy)} + i\varsigma C_{AB,ND}^{(yy)} - \frac{\kappa}{1 - \frac{\kappa}{K_{AR,ND}^{(yy)} - K_{R,ND}\left(\frac{m_{JB,ND}}{2}\right)\kappa + i\varsigma C_{AR,ND}^{(yy)}}}$$

The non-dimensional (ND) DC of AB and AR are:
$K_{\mathrm{AB,ND}}^{(ij)} = c_{\mathrm{AB}} K_{\mathrm{AB}}^{(ij)} / \left(p_{\mathrm{a}} L D_{\mathrm{J}}\right)$
$C_{\mathrm{AB,ND}}^{(ij)} = c_{\mathrm{AB}}\, \omega C_{\mathrm{AB}}^{(ij)} / \left(p_{\mathrm{a}} L D_{\mathrm{J}}\right)$
$K_{\mathrm{AR,ND}}^{(ij)} = c_{\mathrm{AB}} K_{\mathrm{AR}}^{(ij)} / \left(p_{\mathrm{a}} L D_{\mathrm{J}}\right)$ and
$C_{\mathrm{AR,ND}}^{(ij)} = c_{\mathrm{AB}}\, \omega C_{\mathrm{AR}}^{(ij)} / \left(p_{\mathrm{a}} L D_{\mathrm{J}}\right)$
where the superscripts i and j can be x or y. The frequency ratio, ς, and the speed ratio, ϖ are: $\varsigma = \nu/\omega$, $\varpi = \omega/\omega_{\mathrm{n}}$, and the non-dimensional bushing mass, $m_{\mathrm{JB,ND}} = m_{\mathrm{JB}} / \left[\left(L/D_{\mathrm{J}}\right)^2 m_{\mathrm{R}}\right]$. Since the RABDFS and RARBS consist of rigid rotors, the stiffness of the rotor, $K_{\mathrm{R,ND}} = \infty$, $\kappa = (\varpi\varsigma)^2$, and $\varpi = \left[m_{\mathrm{R}} c_{\mathrm{AB}}\, \omega^2 / \left(p_{\mathrm{a}} L D_{\mathrm{J}}\right)\right]^{1/2}$.

In the RABDFS, the bushing is rigidly mounted on the casing. Hence, $K_{\mathrm{AR,ND}}^{(ij)} = \infty$ and $C_{\mathrm{AR,ND}}^{(ij)} = \infty$. Equating the real and the imaginary parts of Eq. (1) to zero,

$$\kappa = \frac{K_{\mathrm{AB,ND}}^{(xx)} C_{\mathrm{AB,ND}}^{(yy)} + K_{\mathrm{AB,ND}}^{(yy)} C_{\mathrm{AB,ND}}^{(xx)} - K_{\mathrm{AB,ND}}^{(xy)} C_{\mathrm{AB,ND}}^{(yx)} - K_{\mathrm{AB,ND}}^{(yx)} C_{\mathrm{AB,ND}}^{(xy)}}{C_{\mathrm{AB,ND}}^{(xx)} + C_{\mathrm{AB,ND}}^{(yy)}} \quad \ldots (2)$$

$$\left(K_{\mathrm{AB,ND}}^{(xx)} - \kappa\right)\left(K_{\mathrm{AB,ND}}^{(yy)} - \kappa\right) - K_{\mathrm{AB,ND}}^{(xy)} K_{\mathrm{AB,ND}}^{(yx)} - \varsigma^2 \left(C_{\mathrm{AB,ND}}^{(xx)} C_{\mathrm{AB,ND}}^{(yy)} - C_{\mathrm{AB,ND}}^{(xy)} C_{\mathrm{AB,ND}}^{(yx)}\right) = 0 \quad \ldots (3)$$

ν in ς is varied over $1 \le \nu \le \nu_{\max}$. κ is computed using Eq. (2) for each ν. If the computed κ at any ν satisfies Eq. (3) then $\nu = \nu_{\mathrm{DSB}}$. $m_{\mathrm{R,C}}$ is computed using $\nu_{\mathrm{DSB}} = \left(K_{\mathrm{B}}/m_{\mathrm{R,C}}\right)^{1/2}$ where the effective stiffness coefficient of bearing, K_{B} is found from $\kappa = c_{\mathrm{AB}} K_{\mathrm{B}} / \left(p_{\mathrm{a}} L D_{\mathrm{J}}\right)$.

In the case of RARBS, Eq. (1) reduces to,

$$C_{\mathrm{B,ND}} = \frac{-\kappa^2 \varsigma C_{\mathrm{AR,ND}}^{(ij)}}{\left[K_{\mathrm{AR,ND}}^{(ij)} - \left(1 + m_{\mathrm{JB,ND}}\right)\kappa\right]^2 + \left(C_{\mathrm{AR,ND}}^{(ij)} \varsigma\right)^2} \quad \ldots (4)$$

$$\kappa = \frac{K_{\mathrm{AR,ND}}^{(ij)} C_{\mathrm{B,ND}} + \varsigma C_{\mathrm{AR,ND}}^{(ij)} K_{\mathrm{B,ND}}}{C_{\mathrm{B,ND}}\left(1 + m_{\mathrm{JB,ND}}\right) + C_{\mathrm{AR,ND}}^{(ij)} \varsigma} \quad \ldots (5)$$

where the effective stiffness coefficient, K_{B} is found using: $K_{\mathrm{B,ND}} = c_{\mathrm{AB}} K_{\mathrm{B}} / \left(p_{\mathrm{a}} L D_{\mathrm{J}}\right)$.

$$E^4 + \left[\begin{array}{l} \frac{1}{4}\left(K_{\mathrm{AB,ND}}^{(xx)} - K_{\mathrm{AB,ND}}^{(yy)}\right)^2 + K_{\mathrm{AB,ND}}^{(xy)} K_{\mathrm{AB,ND}}^{(yx)} \\ -\frac{\varsigma^2}{4}\left(C_{\mathrm{AB,ND}}^{(xx)} - C_{\mathrm{AB,ND}}^{(yy)}\right)^2 - \varsigma^2 C_{\mathrm{AB,ND}}^{(xy)} C_{\mathrm{AB,ND}}^{(yx)} \end{array}\right] E^2 - \left[\frac{\varsigma}{4}\left(K_{\mathrm{AB,ND}}^{(xx)} - K_{\mathrm{AB,ND}}^{(yy)}\right)\left(C_{\mathrm{AB,ND}}^{(xx)} - C_{\mathrm{AB,ND}}^{(yy)}\right) + \frac{\varsigma}{2}\left(\begin{array}{l} K_{\mathrm{AB,ND}}^{(xy)} C_{\mathrm{AB,ND}}^{(yx)} \\ +K_{\mathrm{AB,ND}}^{(yx)} C_{\mathrm{AB,ND}}^{(xy)} \end{array}\right)\right]^2 = 0 \quad \ldots (6)$$

$$K_{\mathrm{B,ND}} = \frac{1}{2}\left\{\left(K_{\mathrm{AB,ND}}^{(xx)} + K_{\mathrm{AB,ND}}^{(yy)}\right) - \frac{\varsigma\left[\left(\frac{K_{\mathrm{AB,ND}}^{(xx)} - K_{\mathrm{AB,ND}}^{(yy)}}{2}\right)\left(C_{\mathrm{AB,ND}}^{(xx)} - C_{\mathrm{AB,ND}}^{(yy)}\right) + \left(\begin{array}{l} K_{\mathrm{AB,ND}}^{(xy)} C_{\mathrm{AB,ND}}^{(yx)} \\ +K_{\mathrm{AB,ND}}^{(yx)} C_{\mathrm{AB,ND}}^{(xy)} \end{array}\right)\right]}{E}\right\}$$

$$C_{\mathrm{B,ND}} = \frac{\varsigma}{2}\left(C_{\mathrm{AB,ND}}^{(xx)} + C_{\mathrm{AB,ND}}^{(yy)}\right) - E$$

Among the four roots of E in Eq. (6), the positive real root is used in the calculation since $K_{\mathrm{B,ND}}$ and $C_{\mathrm{B,ND}}$ are real and positive. ν in ς is varied over $1 \le \nu \le \nu_{\max}$. κ is computed using Eq. (5) for each ν. If the computed κ at any ν satisfies Eq. (4) then $\nu = \nu_{\mathrm{DSB}}$. $m_{\mathrm{R,C}}$ is computed using $\nu_{\mathrm{DSB}} = \left(K_{\mathrm{B}}/m_{\mathrm{R,C}}\right)^{1/2}$.

3 Results and Discussion

3.1 Static and dynamic characteristics of RABDFS and RARBS

3.1.1 Static characteristics

The steady-state simulation (SSS) in a two-degrees-of-freedom approach[25] provides the following: (a) coordinates of the static equilibrium position identified at t = 0, i.e., $\left(X_{\mathrm{J}}(0), Y_{\mathrm{J}}(0)\right)$ of $\mathrm{CG_J}$, and $\left(X_{\mathrm{B}}(0), Y_{\mathrm{B}}(0)\right)$ of $\mathrm{CG_B}$ which can be defined in terms of e and α as $\left(e_{\mathrm{J}}^0, \alpha_{\mathrm{J}}^0\right)$ and $\left(e_{\mathrm{B}}^0, \alpha_{\mathrm{B}}^0\right)$, respectively (Fig. 1); and similarly (b) components of static load-carrying capacity $\left(F_{\mathrm{J}}{}^{(x)}(0), F_{\mathrm{J}}{}^{(y)}(0)\right)$ and $\left(F_{\mathrm{B}}{}^{(x)}(0), F_{\mathrm{B}}{}^{(y)}(0)\right)$. Figures 9 & 10 show the static characteristics of ABDFS and ARB respectively at ω (rad $\mathrm{s^{-1}}$) = 680.7, 1309, 1937.3, 2565.6, and 3193.9. ω is chosen at equal intervals of 628.3 rad $\mathrm{s^{-1}}$ on both sides of $\omega_{\max}$ = 2565.6 rad $\mathrm{s^{-1}}$ that corresponds to $S_{\max}$ = 24500 RPM (see Table 1).

With an increase in ω, it is observed that a static equilibrium position is attained with a decrease in e_{J}^0 for both ABDFS and ARB. With an increase in ω, e_{B}^0

remains constant for ARB. Under purely hydrodynamic lubrication and incompressible flow conditions, e decreases from c to zero as ω increases from zero to infinity (with constant $\alpha_J^0 = \pi/2$).[29] However, from Figs 9 & 10, it is seen that the variations of e_J^0 and α_J^0 over the given range of ω for ABDFS and ARB are smaller. These results suggest that the role of hydrodynamic lubrication may be smaller and the ABDFS and the ARB operate mainly under a hydrostatic lubrication mechanism due to the supply of externally-pressurized air. However, it is observed that the variations of e_J^0 over the given range of ω for ABDFS are greater than the corresponding variations of e_J^0 for ARB (see Figs 9 & 10). These results suggest that the role of hydrostatic lubrication in the ABDFS is smaller in comparison with the ARB. The presence of AR with the chamber feeding system in the ARB characterizes its greater level of hydrostatic lubrication. It is also inferred that both the ABDFS and the ARB show a smaller α_J^0 than a bearing operated with incompressible lubricants.[29]

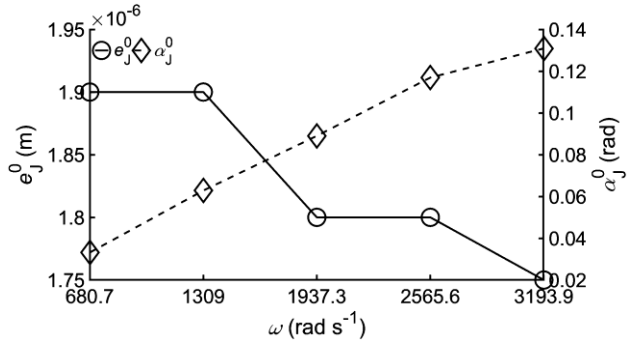

Fig. 9 — Static characteristics of ABDFS (Static equilibrium positions of the journal in terms of eccentricity (e) and attitude angle (α) as (e_J^0, α_J^0) arrived at various angular velocities of the journal, ω. ω is chosen at equal intervals of 628.3 rad s^{-1} on both sides of ω_{max} = 2565.6 rad s^{-1} which corresponds to the maximum rotational speed of the rotor, S_{max} = 24500 RPM. Static equilibrium positions are attained with a decrease in e_J^0 and an increase in α_J^0 as ω is increased. Smaller range of variation of e_J^0 and α_J^0 suggest that ABDFS operates mainly under a hydrostatic lubrication mechanism).

3.1.2 Dynamic coefficients

Figures 11 & 12 show the DC of ABDFS and Figs 13–16 show the DC of ARB at ω (rad s^{-1}) = 680.7, 1309, 1937.3, 2565.6, and 3193.9, ν (rad s^{-1}) = 340.3, 654.5, 968.7, 1282.8, and 1597. ω is chosen at equal intervals of 628.3 rad s^{-1} on both sides of ω_{max} =

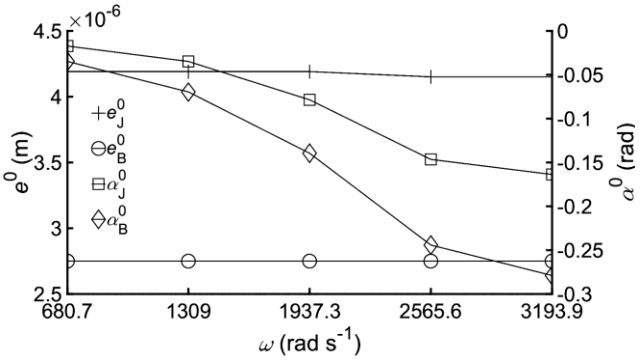

Fig. 10 — Static characteristics of ARB (Static equilibrium positions of the journal (J) and the bushing (B) in terms of eccentricity (e) and attitude angle (α) as (e_J^0, α_J^0) and (e_B^0, α_B^0) arrived at various angular velocities of the journal, ω. ω is chosen at equal intervals of 628.3 rad s^{-1} on both sides of ω_{max} = 2565.6 rad s^{-1} which corresponds to the maximum rotational speed of the rotor, S_{max} = 24500 RPM. Static equilibrium positions are attained with almost a constant e_J^0, a constant e_B^0, and an increase in α_J^0 and α_B^0 as ω is increased. Smaller range of variation of e_J^0, e_B^0, α_J^0, and α_B^0 suggest that ARB operates mainly under a hydrostatic lubrication mechanism).

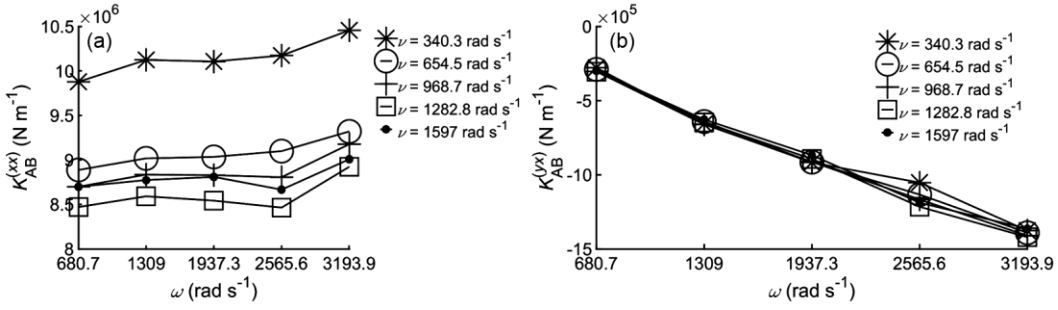

Fig. 11 — (a) Direct and (b) cross-coupled stiffness coefficients of ABDFS ($K_{AB}^{(yx)}$ is 10-times smaller than $K_{AB}^{(xx)}$, implying that harmful hydrodynamic instability conditions are reduced in RABDFS. The stronger dependence of $K_{AB}^{(xx)}$ on ν shows that the squeeze film lubrication mechanism is more predominant. When ν increases from 340.3 rad s^{-1} to 1282.8 rad s^{-1}, the air compressibility softens the ABDFS. When ν increases further from 1282.8 rad s^{-1} to 1597 rad s^{-1}, the air compressibility stiffens or hardens the ABDFS. Thus, there is a decrease of $K_{AB}^{(xx)}$ when ν increases from 340.3 rad s^{-1} to 1282.8 rad s^{-1} and an increase of $K_{AB}^{(xx)}$ when ν increases from 1282.8 rad s^{-1} to 1597 rad s^{-1}. The increasing contribution of the hydrodynamic lubrication mechanism with increasing ω results in an increase of $K_{AB}^{(yx)}$).

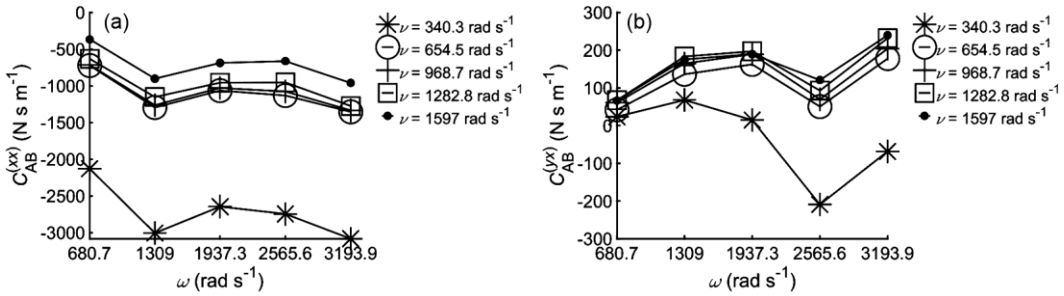

Fig. 12 — (a) Direct and (b) cross-coupled damping coefficients of ABDFS ($C_{AB}^{(yx)}$ is 13-times smaller than $C_{AB}^{(xx)}$, implying that harmful hydrodynamic instability conditions are reduced in RABDFS. $C_{AB}^{(xx)} < 0$. The stronger dependence of $C_{AB}^{(xx)}$ on ν shows that the squeeze film lubrication mechanism is more predominant. When ν increases, the air compressibility makes $C_{AB}^{(xx)}$ to decrease towards zero. The trend indicates that $C_{AB}^{(xx)} \to 0$ as $\nu \to \infty$).

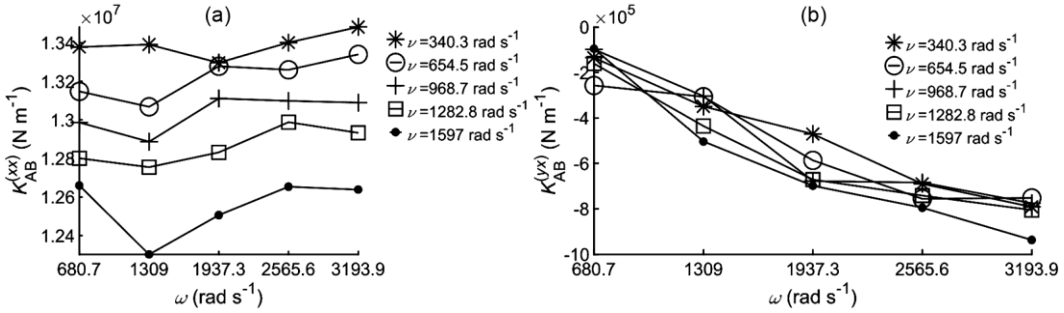

Fig. 13 — (a) Direct and (b) cross-coupled stiffness coefficients of AB in ARB ($K_{AB}^{(yx)}$ is 24-times smaller than $K_{AB}^{(xx)}$, implying that harmful hydrodynamic instability conditions are reduced in RARBS. The stronger dependence of $K_{AB}^{(xx)}$ on ν shows that the squeeze film lubrication mechanism is more predominant. When ν increases, the air compressibility softens the AB of ARB. Thus, there is a decrease of $K_{AB}^{(xx)}$ when ν increases. The increasing contribution of the hydrodynamic lubrication mechanism with increasing ω results in an increase of $K_{AB}^{(yx)}$).

2565.6 rad s^{-1} that corresponds to S_{max} = 24500 RPM (Table 1). Since the problem considered here investigates self-excited vibration or half-frequency whirl, $\nu = \omega/2$ in Figs 11–16.

The following inferences are made from simulation results for ABDFS and ARB shown in Figs 11–16:

a. $K_{AB}^{(yx)}$ is 10-times smaller than $K_{AB}^{(xx)}$ and $C_{AB}^{(yx)}$ is 13-times smaller than $C_{AB}^{(xx)}$ in ABDFS (see Figs 11 & 12). $K_{AB}^{(yx)}$ is 24-times smaller than $K_{AB}^{(xx)}$ and $C_{AB}^{(yx)}$ is 16-times smaller than $C_{AB}^{(xx)}$ in ARB (Figs 13 & 14). $K_{AR}^{(yx)}$ is 86-times smaller than $K_{AR}^{(xx)}$ and $C_{AR}^{(yx)}$ is 46-times smaller than $C_{AR}^{(xx)}$ in ARB (Figs 15 & 16). Smaller cross-coupled coefficients imply that harmful hydrodynamic instability conditions are reduced in both RABDFS and RARBS.

b. $K_{AB}^{(xx)}$ and $C_{AB}^{(xx)}$ of ABDFS are stronger functions of ν when compared to their variations with ω (see Figs 11(a) & 12(a)). $K_{AB}^{(xx)}$, $C_{AB}^{(xx)}$, $K_{AR}^{(xx)}$, and $C_{AR}^{(xx)}$ of ARB are also stronger functions of ν (Figs 13(a), 14(a), 15(a), & 16(a)). The stronger dependence of these DC on ν shows that the squeeze film lubrication mechanism is more predominant in both ABDFS and ARB. As ω increases, $K_{AB}^{(yx)}$ increases and $C_{AB}^{(yx)}$ decreases (Figs 11(b), 12(b), 13(b), & 14(b)). These variations of $K_{AB}^{(yx)}$ and $C_{AB}^{(yx)}$ are attributed to the increasing contribution of hydrodynamic lubrication mechanism with increasing ω in both ABDFS and ARB.

c. The incorporation of AR in ARB results in higher values of the direct DC of AB when compared with the direct DC of AB in ABDFS.[22] $C_{AB}^{(xx)} < 0$ for both the types (Figs 12(a) and 14(a)). These facts are verified in this investigation where (a) the average of direct stiffness coefficients of AB in ARB is 43.07% larger than that of AB in ABDFS, (b) the direct damping coefficients of AB in ARB are 21.97% larger than that of AB in ABDFS.

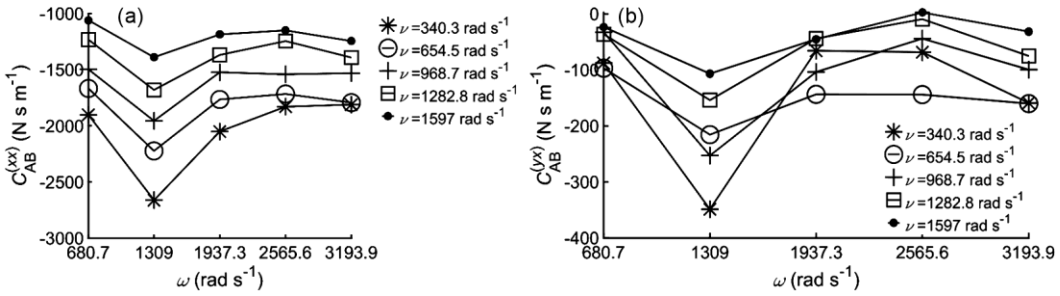

Fig. 14 — (a) Direct and (b) cross-coupled damping coefficients of AB in ARB ($C_{AB}^{(yx)}$ is 16-times smaller than $C_{AB}^{(xx)}$, implying that harmful hydrodynamic instability conditions are reduced in RARBS. $C_{AB}^{(xx)} < 0$. The stronger dependence of $C_{AB}^{(xx)}$ on ν shows that the squeeze film lubrication mechanism is more predominant. When ν increases, the air compressibility makes $C_{AB}^{(xx)}$ to decrease towards zero. The trend indicates that $C_{AB}^{(xx)} \to 0$ as $\nu \to \infty$).

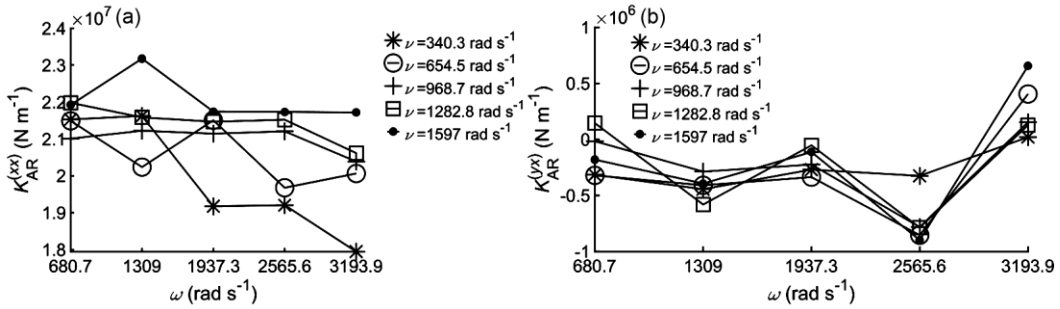

Fig. 15 — (a) Direct and (b) cross-coupled stiffness coefficients of AR in ARB (When ν increases, the air compressibility hardens the AR of ARB. Thus, there is an increase of $K_{AR}^{(xx)}$ when ν increases. Since the bushing does not rotate, there is an absence of the hydrodynamic lubrication mechanism in AR. Thus, with increasing ω, $K_{AR}^{(yx)}$ remains constant).

d. The direct DC of AB in ABDFS and the direct DC of AB and AR in ARB are affected by the fluid compressibility effects.[30] When ν increases from 340.3 rad s^{-1} to 1282.8 rad s^{-1}, the air compressibility softens the AB of ABDFS. When ν increases further from 1282.8 rad s^{-1} to 1597 rad s^{-1}, the air compressibility stiffens or hardens the AB of ABDFS. Thus, there is a decrease of $K_{AB}^{(xx)}$ when ν increases from 340.3 rad s^{-1} to 1282.8 rad s^{-1} and an increase of $K_{AB}^{(xx)}$ when ν increases from 1282.8 rad s^{-1} to 1597 rad s^{-1} in ABDFS (Fig. 11(a)). When ν increases, the air compressibility softens the AB and hardens the AR of ARB. When ν increases, it results in a decrease of $K_{AB}^{(xx)}$ (Fig. 13(a)) and an increase of $K_{AR}^{(xx)}$ for ARB (Fig. 15(a)). When ν increases, the air compressibility makes $C_{AB}^{(xx)}$ of both ABDFS and ARB (Figs 12(a) & 14(a)) and $C_{AR}^{(xx)}$ of ARB (Fig. 16(a)) to decrease towards zero. The trend indicates that $C_{AB}^{(xx)} \to 0$ for both ABDFS and ARB, and $C_{AR}^{(xx)} \to 0$ for ARB, as $\nu \to \infty$.

3.1.3 Comparisons of dynamic stability of RABDFS and RARBS

The DC of ABDFS are determined at all sets of *5* selected values of ω (rad s^{-1}) = 680.7, 1309, 1937.3, 2565.6, and 3193.9 and *5* selected values of ν (rad s^{-1}) = 340.3, 654.5, 968.7, 1282.8, and 1597, in the operating range, using the two-degrees-of-freedom solution procedure[25] (Figs 11 & 12). ω is chosen at equal intervals of 628.3 rad s^{-1} on both sides of ω_{max} = 2565.6 rad s^{-1} that corresponds to S_{max} = 24500 RPM (see Table 1). Since the problem considered here investigates self-excited vibration or half-frequency whirl, $\nu = \omega/2$. The DC of ABDFS at any ω and ν in its operating range are estimated, by following the procedure given by Czołczyński [22] and Muthanandam[28], using these 5×5 sets of DC. Due to the comparatively small journal eccentricity ϵ (e = 1 μm), the calculated values of DC of ABDFS using the two-degrees-of-freedom solution procedure presented by Muthanandam & Thyageswaran[25] fulfill the following relations: $K_{AB}^{(yy)} \approx K_{AB}^{(xx)}$, $K_{AB}^{(xy)} \approx -K_{AB}^{(yx)}$, $C_{AB}^{(yy)} \approx C_{AB}^{(xx)}$, $C_{AB}^{(xy)} \approx -C_{AB}^{(yx)}$. These relations are used in solving equations of free-vibrations of the RABDFS.

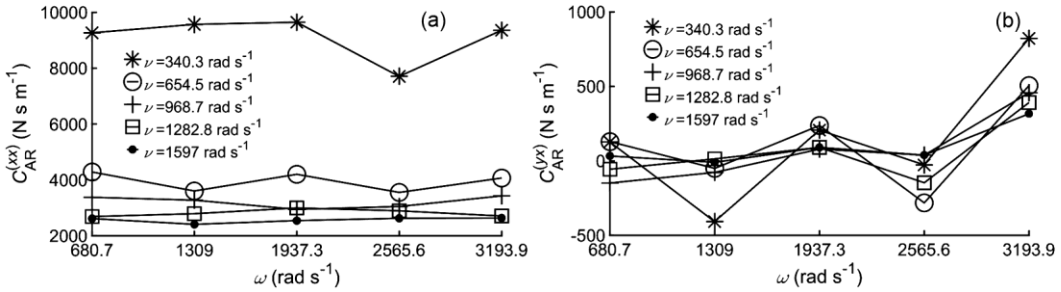

Fig. 16 — (a) Direct and (b) cross-coupled damping coefficients of AR in ARB ($C_{AR}^{(xx)} > 0$. When ν increases, the air compressibility makes $C_{AR}^{(xx)}$ to decrease towards zero. The trend indicates that $C_{AR}^{(xx)} \to 0$ as $\nu \to \infty$. Since the bushing does not rotate, there is an absence of the hydrodynamic lubrication mechanism in AR. Thus, with increasing ω, $C_{AR}^{(yx)}$ remains constant).

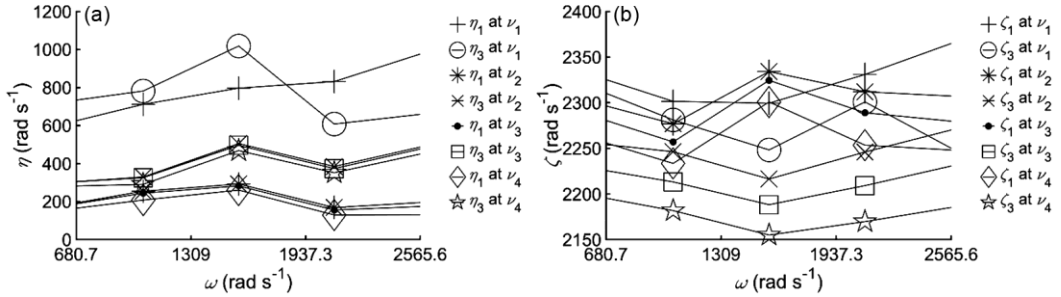

Fig. 17 — (a) Real part, (b) Imaginary part of eigenvalues $\lambda_j = \eta_j + i\zeta_j$ of RABDFS in cylindrical vibrations (ν_1 = 340.3 rad s^{-1}, ν_2 = 654.5 rad s^{-1}, ν_3 = 968.7 rad s^{-1}, and ν_4 = 1282.8 rad s^{-1}).

Since the bushing of an ABDFS is rigidly mounted with the casing (Fig. 4) and for all sets of (ω, ν), $C_{AB}^{(xx)} < 0$ (Fig. 12(a)), the RABDFS is unstable over the entire operating ω range with ω_{max} = 2565.6 rad s^{-1}. This behavior is verified by solving equations of motion in cylindrical vibration mode and by solving equations of motion in conical vibration mode.

Figures 17(a) & 17(b) show the eigenvalues ($\lambda_j = \eta_j + i\zeta_j$, j = 1, 3) of the RABDFS in cylindrical vibration mode. Figures 18(a) & 18(b) show the eigenvalues ($\lambda_j = \eta_j + i\zeta_j$, j = 1, 3) of the RABDFS in conical vibration mode. In Figs 17 & 18, the eigenvalues are shown in the range of 680.7 ≤ ω (rad s^{-1}) ≤ 2565.6 and ν (rad s^{-1}) = 340.3, 654.5, 968.7, and 1282.8.

Since the RABDFS has two degrees of freedom, x_R and y_R (in cylindrical vibration mode), and Ψ_R and Φ_R (in conical vibration mode), there are four eigenvalues $\lambda_j = \eta_j + i\zeta_j$ ($1 \le j \le 4$) obtained by solving equations of motion for each mode of vibration. Every two eigenvalues which correspond to a given degree of freedom, are complex conjugates of each other. i.e., λ_1 and λ_3 are complex conjugates of λ_2 and λ_4 respectively. Hence, a presentation of eigenvalues λ_2 and λ_4 has been avoided. The real part η_j of λ_j determines the rate of damping. In Figs 17(a) & 18(a), it is noted that the real part of the eigenvalue $\eta_j > 0$. This implies that the vibration amplitude increases with time, thus predicting the unstable behavior of the RABDFS at any ω.

When ES (having the DC, $K_{ES}^{(xx)}, K_{ES}^{(yy)}, K_{ES}^{(yx)}, K_{ES}^{(xy)}, C_{ES}^{(xx)}, C_{ES}^{(yy)}, C_{ES}^{(yx)}$, and $C_{ES}^{(xy)}$) is introduced between the bushing and the casing, a condition of $C^{(ij)} > 0$ can be achieved.[22] The ES in the RABDFS is capable of preventing self-excited vibration.

Due to the comparatively small journal eccentricity ϵ (e = 1 μm), the calculated values of DC of ABDFS with ES fulfill the following relations: $K_{ES}^{(yy)} \approx K_{ES}^{(xx)}, K_{ES}^{(xy)} \approx K_{ES}^{(yx)}, C_{ES}^{(yy)} \approx C_{ES}^{(xx)}, \quad C_{ES}^{(xy)} \approx C_{ES}^{(yx)}$. These relations are used in solving equations of free vibrations where the DC of AR is replaced with the DC of ES. Maps of DC are arrived at by solving these equations with ω_{max} = 2565.6 rad s^{-1} and $\nu_{max} = \omega_{max}/2$. It is found that the effect of cross-coupled DC on the dynamic stability of the RABDFS is negligible when compared with the effect of direct DC. Hence, the maps of direct DC of ES only are presented.

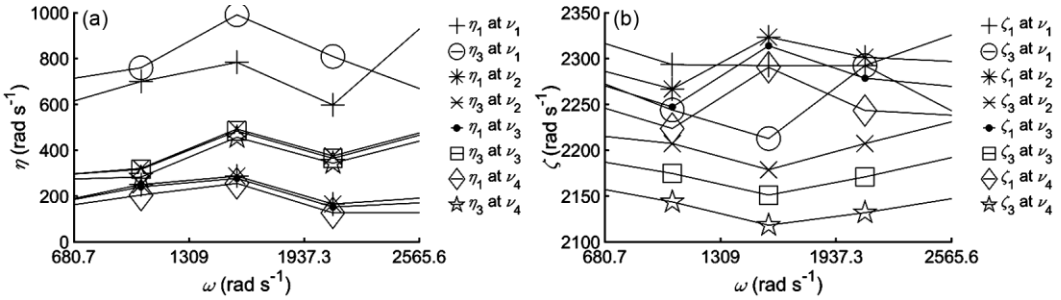

Fig. 18 — (a) Real part, (b) Imaginary part of eigenvalues $\lambda_j = \eta_j + i\zeta_j$ of RABDFS in conical vibrations (ν_1 = 340.3 rad s^{-1}, ν_2 = 654.5 rad s^{-1}, ν_3 = 968.7 rad s^{-1}, and ν_4 = 1282.8 rad s^{-1}).

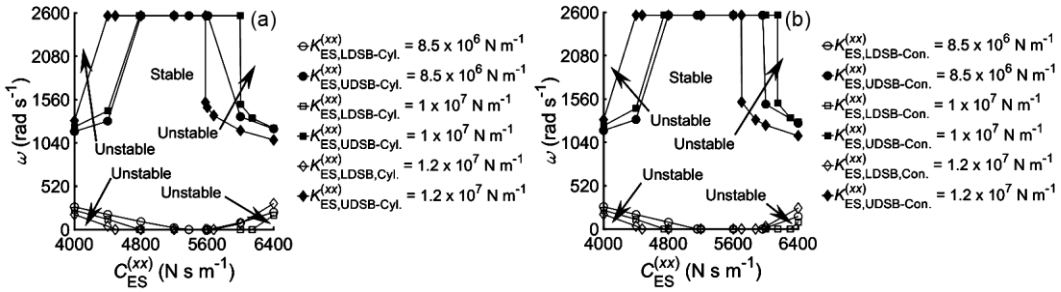

Fig. 19 — Type 1 dynamic stability maps of RABDFS. (a) Cylindrical vibrations. (b) Conical vibrations (Dynamic stability boundaries (DSB) distinguish the dynamically stable region from the dynamically unstable region. For a given DC of ES for the bushing, LDSB and UDSB dictate the stable lower operating ω limit and the stable upper operating ω limit, respectively).

Since the DC of AB only are known at all ω and ν in the range of $1 \le \omega$ (rad s^{-1}) ≤ 2565.6 and $1 \le \nu$ (rad s^{-1}) ≤ 1282.8, type 1 dynamic stability maps (Figs 19 & 20) are arrived at by following the calculation procedure given in the section 2.1.5. The dynamically stable region is distinguished from the dynamically unstable region using the dynamic stability boundaries (DSB) in Figs 19 & 20. The solutions of equations of motion in cylindrical vibration mode result in the DSB in cylindrical vibration mode (DSB-Cyl). By solving equations of motion in conical vibration mode, the DSB in conical vibration mode (DSB-Con) is arrived at.

There are two distinct stability boundaries in Figs 19(a) & 19(b). In Fig. 19(a), LDSB-Cyl and UDSB-Cyl dictate the stable lower operating ω limit and the stable upper operating ω limit, for a given DC $\left(K_{\mathrm{ES}}^{(xx)}, C_{\mathrm{ES}}^{(xx)}\right)$ of ES for the bushing, during the cylindrical vibration mode. In Fig. 19(b), LDSB-Con and UDSB-Con dictate the stable lower operating ω limit and the stable upper operating ω limit, for a given DC $\left(K_{\mathrm{ES}}^{(xx)}, C_{\mathrm{ES}}^{(xx)}\right)$ of ES for the bushing, during the conical vibration mode.

For any given $K_{\mathrm{ES}}^{(xx)}$, there are limits of $C_{\mathrm{ES}}^{(xx)}$ in between which the RABDFS is stable over the entire

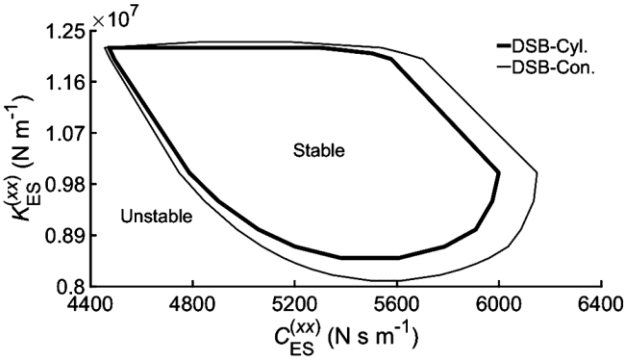

Fig. 20 — Type 1 dynamic stability maps of RABDFS (Dynamic stability boundaries (DSB) distinguish the dynamically stable region from the dynamically unstable region. DSB-Cyl and DSB-Con dictate the range of DC of ES for stable operation of RABDFS during cylindrical vibration mode and conical vibration mode, respectively).

operating ω range with $\omega_{\max}$ = 2565.6 rad s^{-1}. When $C_{\mathrm{ES}}^{(xx)}$ is either decreased or increased beyond these limits, the stable operating range of ω is reduced, for any given $K_{\mathrm{ES}}^{(xx)}$. The stable region can be reached only by passing through a region of instability. Figure 20 dictates the range of $K_{\mathrm{ES}}^{(xx)}$ and $C_{\mathrm{ES}}^{(xx)}$ for which the RABDFS is dynamically stable over the entire operating ω range with $\omega_{\max}$ = 2565.6 rad s^{-1}, for the calculated DC, $K_{\mathrm{AB}}^{(xx)}, K_{\mathrm{AB}}^{(yx)}, C_{\mathrm{AB}}^{(xx)}$, and $C_{\mathrm{AB}}^{(yx)}$. For a

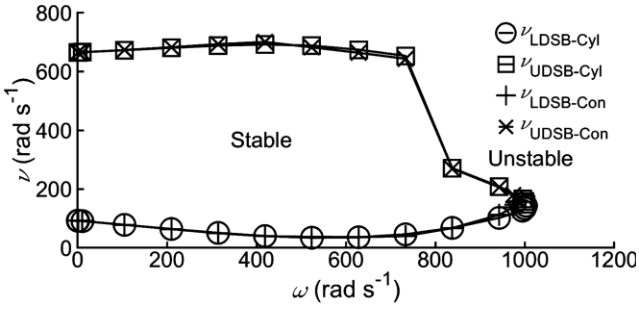

Fig. 21 — Type 2 dynamic stability maps of RARBS (Dynamic stability boundaries (DSB) distinguish the dynamically stable region from the dynamically unstable region. For a given ω, LDSB and UDSB dictate the stable lower operating ν limit and the stable upper operating ν limit, respectively. DSB-Cyl and DSB-Con are found by substituting the DC of AB ($K_{AB}^{(xx)}, K_{AB}^{(yx)}, C_{AB}^{(xx)}$, and $C_{AB}^{(yx)}$) and the DC of AR ($K_{AR}^{(xx)}, K_{AR}^{(yx)}$, $C_{AR}^{(xx)}$, and $C_{AR}^{(yx)}$) in equations of cylindrical vibrations and equations of conical vibrations, respectively. These DC of AB and AR are functions of ω and ν).

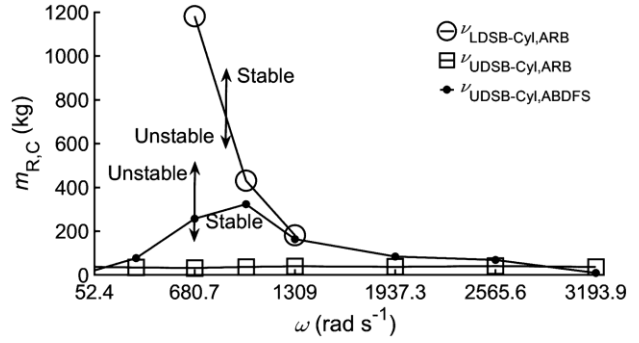

Fig. 22 — Rotor critical mass and stability threshold speeds of RARBS and RABDFS in cylindrical vibrations (At ω = 680.7 rad s^{-1}, RABDFS is stable if $m_R \leq 256.99$ kg, $C_{AB}^{(xx)} > 0$, and $C_{AB}^{(yy)} > 0$. At ω = 680.7 rad s^{-1}, RARBS is stable either if $m_R \geq 1181.43$ kg or if $m_R \leq 32.05$ kg. Since RARBS has m_R = 3.4 kg, its ω_{DSB} = 1002.7 rad s^{-1}. For a given ω = 680.7 rad s^{-1}, $m_{R,C}$ is lower for RARBS when compared with RABDFS).

given RABDFS to be dynamically stable, the DC of ES should lie within their respective stable regions for both vibration modes. Thus, the dynamic stability of a given RABDFS (when an ES is introduced between the bushing and the casing) is verified using the stability maps.

Figure 21 shows type 2 dynamic stability maps of RARBS (Table 1) in both cylindrical vibration mode and conical vibration mode. Figure 22 shows the variation of rotor critical mass ($m_{R,C}$) with ω_{DSB}, and Fig. 23 shows the variation of whirl frequency (ν_{DSB}) with ω_{DSB} of RARBS in cylindrical vibration mode.

The DC of ARB are determined at all sets of *5* selected values of ω (rad s^{-1}) = 680.7, 1309, 1937.3, 2565.6, and 3193.9 and *5* selected values of ν (rad s^{-1}) = 340.3, 654.5, 968.7, 1282.8, and 1597, in the operating range, using the two-degrees-of-freedom solution procedure[25] (see Figs 13–16). The DC of ARB at any ω and ν in its operating range are estimated, by following the procedure given by Czołczyński [22] and Muthanandam[28], using these 5×5 sets of DC. Due to the comparatively small journal eccentricity ϵ (e = 1 μm), the calculated values of DC for ARB using the two-degrees-of-freedom solution procedure presented by Muthanandam & Thyageswaran[25] fulfill the following relations: $K_{AB}^{(yy)} \approx K_{AB}^{(xx)}, K_{AB}^{(xy)} \approx -K_{AB}^{(yx)}, C_{AB}^{(yy)} \approx C_{AB}^{(xx)}, C_{AB}^{(xy)} \approx -C_{AB}^{(yx)}, K_{AR}^{(yy)} \approx K_{AR}^{(xx)}, K_{AR}^{(xy)} \approx K_{AR}^{(yx)}, C_{AR}^{(yy)} \approx C_{AR}^{(xx)}, C_{AR}^{(xy)} \approx C_{AR}^{(yx)}$. These relations are used in solving equations of free-vibrations of the RARBS.

Since the DC of AB and AR are known at all ω and ν in the range of $1 \leq \omega$ (rad s^{-1}) ≤ 2565.6 and $1 \leq \nu$ (rad s^{-1}) ≤ 1282.8, type 2 dynamic stability maps (Fig. 21) are arrived at by following the calculation procedure given in the section of 2.1.5, i.e., maps of ω and ν are arrived at by solving equations of motion. The dynamically stable region is distinguished from the dynamically unstable region using the dynamic stability boundaries (DSB) in Fig. 21. The solutions of equations of motion in cylindrical vibration mode result in the DSB in cylindrical vibration mode (DSB-Cyl). By solving equations of motion in conical vibration mode, the DSB in conical vibration mode (DSB-Con) is arrived at.

There are two distinct stability boundaries for RARBS in Figs 21 & 22. In Figs. 21 and 22, LDSB-Cyl and UDSB-Cyl dictate the stability threshold lower operating ν limit (ν_{LDSB}) and the stability threshold upper operating ν limit (ν_{UDSB}), for a given ω, during the cylindrical vibration mode in RARBS and RABDFS. The stable region can be reached only by passing through a region of instability. Stability threshold lower operating ν limit is not found in RABDFS. Since RARBS consists of an additional bushing mass, m_{JB}, there is an additional stability threshold.[3] In Fig. 21, LDSB-Con and UDSB-Con dictate ν_{LDSB} and ν_{UDSB}, for a given ω, during the conical vibration mode in RARBS. Figure 21 dictates the range of ω and ν, for which the RARBS is dynamically stable, for the calculated DC, $K_{AB}^{(xx)}$, $K_{AB}^{(yx)}$, $C_{AB}^{(xx)}$, $C_{AB}^{(yx)}$, $K_{AR}^{(xx)}$, $K_{AR}^{(yx)}$, $C_{AR}^{(xx)}$, and

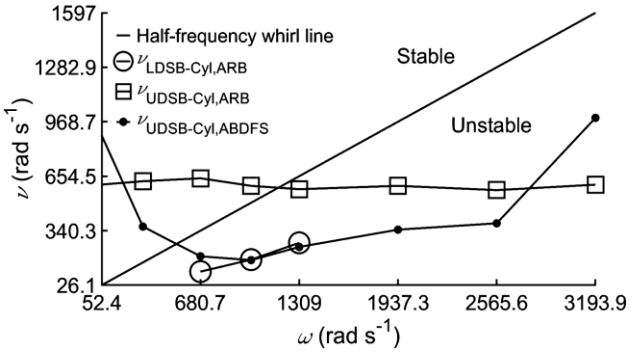

Fig. 23 — Whirl frequency and stability threshold speeds of RARBS and RABDFS in cylindrical vibrations (For RABDFS, ω_{DSB} = 314.2 rad s^{-1} which corresponds to ν_{DSB} = 363.8 rad s^{-1} and $m_{R,C}$ = 77.2 kg. Since m_R = 3.4 kg (Table 1) and $C_{AB}^{(xx)} < 0$ (Fig. 12(a)), the RABDFS is unstable over the entire operating ω range. For RARBS, ω_{DSB} = 1002.7 rad s^{-1} corresponds to ν_{DSB} = 598.89 rad s^{-1}. ς = 0.5973 at this condition. Since $\varsigma > 0.5$ in $1 \le \omega$ (rad s^{-1}) $\le$ 1002.7, RARBS is stable up to ω = 1002.7 rad s^{-1}).

$C_{AR}^{(yx)}$. For the given RARBS to be dynamically stable, ω and ν should lie within their respective stable regions in Fig. 21, for both vibration modes.

Figure 22 shows the maximum speed (ω_{DSB}) that can be achieved for a given rotor mass ($m_{R,C}$). If this speed is exceeded then the self-excited vibration occurs and the rotor system becomes unstable. On the other hand, Fig. 22 dictates the range of m_R for which the rotor system is stable. For the RABDFS and the RARBS to be dynamically stable during cylindrical vibrations, m_R of these two systems should lie within their respective stable regions in Fig. 22. In Fig. 22, $m_{R,C}$ = 256.99 kg corresponds to $\nu_{UDSB-Cyl}$ = 192.47 rad s^{-1} (see Fig. 23) at ω_{DSB} = 680.7 rad s^{-1} for RABDFS. For the RABDFS to be stable, $m_R \le$ 256.99 kg, provided $C_{AB}^{(xx)} > 0$ and $C_{AB}^{(yy)} > 0$. In Fig. 22, $m_{R,C}$ = 1181.43 kg corresponds to $\nu_{LDSB-Cyl}$ = 104.2 rad s^{-1} (Fig. 21) and $m_{R,C}$ = 32.05 kg corresponds to $\nu_{UDSB-Cyl}$ = 642.56 rad s^{-1} (Fig. 21) at ω_{DSB} = 680.7 rad s^{-1} for RARBS. For a given ω_{DSB} = 680.7 rad s^{-1}, $m_{R,C}$ is lower for RARBS when compared with RABDFS. For the RARBS to be stable, either $m_R \ge$ 1181.43 kg or $m_R \le$ 32.05 kg. Since RARBS has m_R = 3.4 kg, its ω_{DSB} = 1002.7 rad s^{-1}, as explained below.

The two extreme conditions of $\nu_{LDSB-Cyl}$ and $\nu_{UDSB-Cyl}$ in RARBS correspond to two different whirl frequency ratios ς_{min} = 0.1531 and ς_{max} = 0.944. In the first case, the journal executes 108 revolutions while the CG_J completes only 17 revolutions in one second. Since the CG_J orbits at a rate that is much slower than the journal rotation rate, the orbital motion of CG_J does not make any significant change in the pressure distribution in the RARBS. During this whirl condition, the CG_J occupies successive static equilibrium positions (e_J^0, α_J^0) and the self-excited whirl develops.

In the second case, the journal executes 108 revolutions while the CG_J completes only 102 revolutions in one second. Since the CG_J orbits at a rate that is nearer to and slightly lesser than the journal rotation rate, the orbital motion of CG_J makes significant changes in the pressure distribution that effectively damps the motion of the RARBS.

Thus, it is inferred from Fig. 23 that a self-excited whirl develops when $\nu < \omega/2$. From Fig. 23, for RARBS, ω_{DSB} = 1002.7 rad s^{-1} corresponds to ν_{DSB} = 598.89 rad s^{-1}. ς = 0.5973 at this condition. Since $\varsigma > 0.5$ in $1 \le \omega$ (rad s^{-1}) $\le$ 1002.7, RARBS is stable up to ω = 1002.7 rad s^{-1}. However, the stable region can be reached only by passing through a region of instability as shown in Fig. 21. Since $\varsigma < 0.5$ in 1309 $\le \omega$ (rad s^{-1}) $\le$ 3193.9, RARBS is unstable from ω = 1309 rad s^{-1} to 3193.9 rad s^{-1}.

In Figs 22 & 23, for RABDFS, ω_{DSB} = 314.2 rad s^{-1} which corresponds to ν_{DSB} = 363.8 rad s^{-1} and $m_{R,C}$ = 77.2 kg. ς = 1.1579 at this condition. Since $\varsigma >$ 0.5 in $1 \le \omega$ (rad s^{-1}) $\le$ 314.2, RABDFS will be stable up to ω = 314.2 rad s^{-1}, provided $m_{R,C}$ = 77.2 kg, $C_{AB}^{(xx)} > 0$ and $C_{AB}^{(yy)} > 0$. Since $\varsigma < 0.5$ in 680.7 $\le \omega$ (rad s^{-1}) $\le$ 3193.9, RABDFS with $m_{R,C}$ = 77.2 kg, $C_{AB}^{(xx)} > 0$ and $C_{AB}^{(yy)} > 0$ will be unstable from ω = 680.7 rad s^{-1} to 3193.9 rad s^{-1}. Since m_R = 3.4 kg (Table 1) and $C_{AB}^{(xx)} < 0$ (Fig. 12(a)), the RABDFS is unstable over the entire operating ω range with ω_{max} = 2565.6 rad s^{-1} (which corresponds to the maximum rotor speed, S_{max}).

Incorporation of AR in RARBS results in a larger ω_{DSB} (Fig. 23) and a smaller $m_{R,C}$ (Fig. 22) when compared with RABDFS. Thus, it is verified using the stability maps that the AR element of the ARB is capable of preventing self-excited vibration in lightly loaded rotor-bearing systems.

4 Conclusion

To ascertain the need for an air-ring (AR) in an air-bearing (AB), a comparative study of the dynamic stability of the rotor supported by the following types of air-bearings is carried out: (a) air-bearing with a direct feeding system

(ABDFS) and (b) air-ring bearing (ARB). In the ABDFS, (i) there is no AR and the bushing is rigidly fixed to the casing and (ii) there is no air chamber and the air is fed into AB directly through the orifice.

The following inferences are made from the steady-state simulation and the transient-state simulation at [ω (rad s^{-1}), ν (rad s^{-1})] = (680.7, 340.3), (1309, 654.5), (1937.3, 968.7), (2565.6, 1282.8), and (3193.9, 1597)] for ABDFS and ARB: Both the ABDFS and the ARB operate mainly under a hydrostatic lubrication mechanism due to the supply of externally-pressurized air. However, the presence of AR with the chamber feeding system in the ARB characterizes its greater level of hydrostatic lubrication. The stronger dependence of the direct DC on ν shows that the squeeze film lubrication mechanism is more predominant in both the ABDFS and the ARB. The average of direct stiffness coefficients of AB in ARB is 43.07% larger than that of AB in ABDFS and the average of direct damping coefficients of AB in ARB is 21.97% larger than that of AB in ABDFS. Incorporation of AR in ARB results in higher values of the direct DC of AB when compared with the direct DC of AB in ABDFS. The direct DC of AB in ABDFS and the direct DC of AB and AR in ARB are affected by ν due to the fluid compressibility effects. When ν increases from 340.3 rad s^{-1} to 1282.8 rad s^{-1}, the air compressibility softens the AB of ABDFS. A further increase in ν from 1282.8 rad s^{-1} to 1597 rad s^{-1} stiffens or hardens the AB of ABDFS. Thus, there is a decrease of direct stiffness coefficients of AB when ν increases from 340.3 rad s^{-1} to 1282.8 rad s^{-1} and an increase of direct stiffness coefficients of AB when ν increases from 1282.8 rad s^{-1} to 1597 rad s^{-1} in ABDFS. When ν increases, the air compressibility softens the AB and hardens the AR of ARB. When ν increases, it results in a decrease of direct stiffness coefficients of AB and an increase of direct stiffness coefficients of AR for ARB. When ν increases, the direct damping coefficients of AB of ABDFS and the direct damping coefficients of AB and AR of ARB decrease towards zero.

The dynamic stability is verified using the dynamic stability maps of dynamic coefficients (DC) of air-bearings. These maps are arrived at by solving equations of free-vibration of the rotor AB systems using the DC determined by the two degrees of freedom approach. It is found that the effect of cross-coupled DC on dynamic stability is negligible when compared with the effect of direct DC. The complete dynamic stability analyses of these two rotor AB systems require the determination of DC at all angular velocities of journal ω and journal vibration frequencies ν in the operating range. The results of comparative studies on the dynamic stability of ABDFS and ARB are as follows.

Since the bushing of an ABDFS is rigidly mounted with the casing, the rotor air-bearing with a direct feeding system is unstable over the entire operating ω range. The dynamic stability of the rotor AB system is improved with ARB where the AR acts as flexible, damped support. The rotor air-ring bearing system is dynamically stable up to ω = 1002.7 rad s^{-1}. The rotor critical mass of ARB is smaller than that of ABDFS. Thus, the AR element of the ARB is capable of preventing self-excited vibration in lightly loaded rotor-bearing systems.

At the design stage of ARB, the nominal levels of the ARB parameters such as the mass of the rotor, the mass of the joint-bushing, the diameter of the journal, length of the journal, clearance of air-bearing, clearance of air-ring, air supply pressure, feed-hole orifice diameter, feed-hole chamber diameter, and feed-hole chamber depth, and the deviations from their nominal levels are proposed to be selected based on a computer-aided parameter design. The stiffness coefficients and damping coefficients of ARB calculated using the two-degrees of freedom approach presented in this paper are proposed to be validated by the values calculated using the measured displacements, and force components during the experimentation on ARB. The stability threshold speed of rotation of the journal and the stability map arrived at by numerical simulation on ARB presented in this paper are proposed to be validated by the stability map arrived at by experimentation on ARB.

Acknowledgements

The author wishes to thank Dr. Sridhar Thyageswaran, Professor (Retd.), Department of Mechanical Engineering, Coimbatore Institute of Technology, India, Dr. Pranab Samanta, Principal Scientist, Department of Surface Engineering and Tribology, CSIR-Central Mechanical Engineering Research Institute, India, and Dr. Grzegorz Żywica, Head of the Turbine Dynamics and Diagnostics Department, Institute of Fluid Flow Machinery, Polish Academy of Sciences, Poland, for their comments to improve the contents of this manuscript.

References

1 Pan C H T & Sternlicht B, *Trans ASME J Basic Eng*, 84 (1962) 152.
2 Gross W A, *Trans ASME J Basic Eng*, 84 (1962) 132.
3 Lund J W, *Trans ASME J Appl Mech*, 32 (1965) 911.
4 Chu T Y, McCabe J T & Elrod H G, *Trans ASME J Lubr Technol*, 90 (1968) 162.
5 Powell J W & Tempest M C, *Trans ASME J Lubr Technol*, 90 (1968) 701.
6 Fuller D D, *Trans ASME J Lubr Technol*, 91 (1969) 1.
7 Marsh H, *Trans ASME J Lubr Technol*, 91 (1969) 113.
8 Majumdar B C, *Tribol Int*, 8 (1975) 127.
9 Guha S K, Rao N S & Majumdar B C, *Trans ASME J Tribol*, 110 (1988) 139.
10 Otsu Y, Somaya K & Yoshimoto S, *Tribol Int*, 44 (2011) 9.
11 Bonello P & Pham H, *Nonlinear dynamic analysis of a turbocharger on foil-air bearings with focus on stability and self-excited vibration* (Proceedings of the ASME Turbo Expo: Power for Land, Sea, and Air: Turbine Technical Conference and Exposition, Dusseldorf, Germany), 2014, V07BT32A003.
12 Arghir M, Hassini M A, Balducchi F & Gauthier R, *Trans ASME J Eng Gas Turbines Power*, 138 (2016) 021602.
13 Xiao H, Li W, Zhou Z, Huang X & Ren Y, *Tribol Int*, 120 (2018) 476.
14 Gao Q, Chen W, Lu L, Huo D & Cheng K, *Tribol Int*, 135 (2019) 1.
15 Zeise P & Schweizer B, *J Sound Vib*, 521 (2022) 116392.
16 Brzeski L & Kazimierski Z, *Trans ASME J Lubr Technol*, 101 (1979) 520.
17 Kazimierski Z & Trojnarski J, *Trans ASME J Lubr Technol*, 102 (1980) 59.
18 Czołczyński K, Brzeski L & Kazimierski Z, *Wear*, 167 (1993) 49.
19 Czołczyński K, *Wear*, 201 (1996) 265.
20 Czołczyński K, Kapitaniak T & Marynowski K, *Wear*, 199 (1996) 100.
21 Czołczyński K, *Wear*, 210 (1997) 220.
22 Czołczyński K, *Rotor dynamics of gas-lubricated journal bearing systems*, (Springer-Verlag, New York) 1999.
23 Muthanandam M, Ramamurthy S & Nadarajan S, *Design of air bearing for high speed micro gas turbine* (Proceedings of the 5th National Seminar and Exhibition on Aerospace and related Mechanisms, ISRO Satellite Centre, Bangalore, India), 2005, 269.
24 Muthanandam M, Thyageswaran S, Aswin V & Rajakumaran T, *Analysis of load-carrying abilities in rotor-bearing systems*, paper presented at 13th International Conference on Vibration Problems, Indian Institute of Technology, Guwahati, India, 2017.
25 Muthanandam M & Thyageswaran S, *J Vib Eng Technol*, 9 (2021) 1.
26 https://ntrs.nasa.gov/api/citations/19780010517/downloads/19780010517.pdf (21 May 2021).
27 Al-Bender F, Colombo F, Reynaerts D, Villavicencio R & Waumans T, *Adv Tribol*, 2017 (2017) 1.
28 Muthanandam M, *Self-excited vibration analysis of a rotor air-ring bearing via a two-degrees of freedom approach*. Ph.D. Thesis, Anna University, Chennai, 2021.
29 Khonsari M M & Booser R E, *Applied tribology, bearing design, and lubrication*, (John Wiley and Sons, New York) 2001.
30 http://repository.tamu.edu/handle/1969.1/93197 (26 August 2015).